INTERNATIONAL JOURNAL FOR NUMERICAL METHODS IN FLUIDS
Int. J. Numer. Meth. Fluids **29**: 311–341 (1999)

THREE-DIMENSIONAL EFFECTS IN DYNAMICALLY LOADED JOURNAL BEARINGS

X.K. LI[a], D.RH. GWYNLLYW[b], A.R. DAVIES[b] AND T.N. PHILLIPS[b],*

[a] *Department of Mathematics, De Montfort University, Leicester LE1 9BH, UK*
[b] *Department of Mathematics, University of Wales, Aberystwyth SY23 3BZ, UK*

SUMMARY

The effects of non-Newtonian lubricants on the dynamics of a 3D journal bearing are investigated using a moving spectral element method. Comparisons are made with the findings reported for the 2D case. The variation of L/D, the ratio of the length of the bearing to its diameter, is shown to have a significant effect on the stability properties of the journal. Copyright © 1999 John Wiley & Sons, Ltd.

KEY WORDS: 3D journal bearings; lubrication; spectral element model

1. INTRODUCTION

The study of journal bearing lubrication has, over the years, generated much interest from major oil industries and engine manufacturers alike. In these application areas it is important to predict and assess the performance of lubricants within a journal bearing with respect to wear and efficiency under a wide range of operating conditions. There are many criteria that need to be taken into account in the modelling of the lubricant. Some of the most important are viscoelasticity, oil feed, thermal effects, cavitation, changes in viscosity with shear-rate, temperature and pressure and 3D effects in dynamically loaded journal bearing. Although, in the final analysis, it is an understanding of the combined effects of these phenomena which will be of greatest interest to the lubrication manufacturers, the investigation of individual effects is essential in the development of this understanding. In this paper we investigate the effect of the third dimension on the dynamics of a journal bearing.

The traditional approach to the study of journal bearing lubrication has been via the lubrication approximation introduced by Reynolds [1]. This enables an equation for the pressure within the thin film region of the geometry to be written separately from the kinematical and constitutive equations describing the flow of the lubricant, thereby simplifying greatly the calculation of the reaction forces engendered by the lubricant. Whereas the effectiveness of the lubrication approximation has been supported by experimental evidence in a very wide range of lubrication studies, there are at least two contexts in which the approximation may be open to question. The first is in predicting the fine details of the non-linear dynamics of the journal bearing. Here, the precise pressure boundary conditions exploited in the Reynolds equation can have a profound effect on the dynamics of the journal. The second context is in studying the role of viscoelasticity in journal bearing lubrication.

---

* Correspondence to: Department of Mathematics, University of Wales, Aberystwyth SY23 3BZ, UK.

CCC 0271–2091/99/030311–31$17.50

Received October 1997
Revised March 1998

If the lubrication approximation is not invoked, there is no option but to solve the full set of coupled equations governing the flow of the lubricant, taking proper account of the moving parts of the geometry. Until recently this task has proved too formidable a calculation, but with current computing power combined with efficient and accurate numerical methods, the calculation may be attempted. Here we use the spectral element method to discretise the governing equations and the preconditioned conjugate gradient (PCG) method to solve the resulting system of algebraic equations. A dynamically chosen preconditioner is used to accelerate the convergence of the linear solver.

In this paper we consider the flow of a non-Newtonian lubricant under dynamic loading conditions. In earlier work Gwynllyw *et al.* [2] considered the long bearing approximation in which everything is assumed to be constant along the axis of the bearing. We now remove this assumption and investigate the effect of the third dimension on the stability properties of the journal. We show that changing the length of the journal, keeping all other parameters constant, can have a profound effect on the path of the journal and hence on the minimum oil film thickness within the bearing. These considerations are important for the automotive engineer who is often constrained by the size of the crankshaft when designing motor engines but has a certain amount of freedom in choosing the length of the journal.

For the 2D model of the journal bearing there is a fundamental question which needs to be answered. Namely, where should the arbitrary level of pressure be specified. For a piezoviscous lubricant or a constant viscosity lubricant with cavitation incorporated into the model, the point at which this level is set influences the path of the journal. Gwynllyw *et al.* [2] use short bearing lubrication theory to determine where to set the pressure to zero. For the 3D model this is no longer a problem since the lubricant is at atmospheric pressure at the ends of the bearing.

2. MATHEMATICAL MODEL OF JOURNAL BEARING

The complexity of the dynamically loaded journal bearing problem is only too evident if one considers a lubricant in the 3D region between two eccentric cylinders, where the inner cylinder (the journal) rotates and is also free to move under a time-dependent load, while the outer cylinder (the bearing) is stationary. In the following sections, the geometry of the journal bearing and a full set of coupled equations governing the flow of the lubricant are presented.

2.1. The geometry

Consider the 3D geometry shown schematically in Figure 1. The journal of radius R_J rotates with a constant angular velocity ω in a stationary bearing of radius R_B. Both the journal and the bearing are assumed to be of the same length L in the axial direction (along the z-direction). A parameter of interest, particularly, when making comparisons with lubrication theory, is L/D, where $D = 2R_B$ is the diameter of the bearing. The axes of the journal and the bearing are separated by a distance e, and it is customary to define an eccentricity ratio

$$\varepsilon = \frac{e}{c}, \tag{2.1}$$

where $c = R_B - R_J$, so that $0 \leq \varepsilon \leq 1$.

The region between the journal and the bearing is occupied by a fluid lubricant. For the case of a static load this can be achieved by the fluid motion in a manner that requires no motion of the centre of the journal, it remains in its static equilibrium position. However, in the case of a dynamic load the centre of the journal is no longer stationary but moves freely in response to forces imparted upon it. Such forces consist of the lubricant reaction force on the journal and also an applied load. The latter will be the subject which this paper addresses.

2.2. Equations of fluid motion

The momentum, continuity and constitutive equations for the 3D incompressible flow of a generalized Newtonian fluid are given as follows:

- three momentum equations

$$\rho\left(\frac{\partial u}{\partial t}+u\frac{\partial u}{\partial x}+v\frac{\partial u}{\partial y}+w\frac{\partial u}{\partial z}\right)+\frac{\partial p}{\partial x}-\left(\frac{\partial \tau_{xx}}{\partial x}+\frac{\partial \tau_{xy}}{\partial y}+\frac{\partial \tau_{xz}}{\partial z}\right)=0, \tag{2.2}$$

$$\rho\left(\frac{\partial v}{\partial t}+u\frac{\partial v}{\partial x}+v\frac{\partial v}{\partial y}+w\frac{\partial v}{\partial z}\right)+\frac{\partial p}{\partial y}-\left(\frac{\partial \tau_{xy}}{\partial x}+\frac{\partial \tau_{yy}}{\partial y}+\frac{\partial \tau_{yz}}{\partial z}\right)=0, \tag{2.3}$$

$$\rho\left(\frac{\partial w}{\partial t}+u\frac{\partial w}{\partial x}+v\frac{\partial w}{\partial y}+w\frac{\partial w}{\partial z}\right)+\frac{\partial p}{\partial z}-\left(\frac{\partial \tau_{xz}}{\partial x}+\frac{\partial \tau_{yz}}{\partial y}+\frac{\partial \tau_{zz}}{\partial z}\right)=0; \tag{2.4}$$

- the scalar conservation of mass equation

$$\frac{\partial u}{\partial x}+\frac{\partial v}{\partial y}+\frac{\partial w}{\partial z}=0; \tag{2.5}$$

- six constitutive equations

$$\tau_{xx}=2\eta\frac{\partial u}{\partial x}, \tag{2.6}$$

$$\tau_{yy}=2\eta\frac{\partial v}{\partial y}, \tag{2.7}$$

$$\tau_{zz}=2\eta\frac{\partial w}{\partial z} \tag{2.8}$$

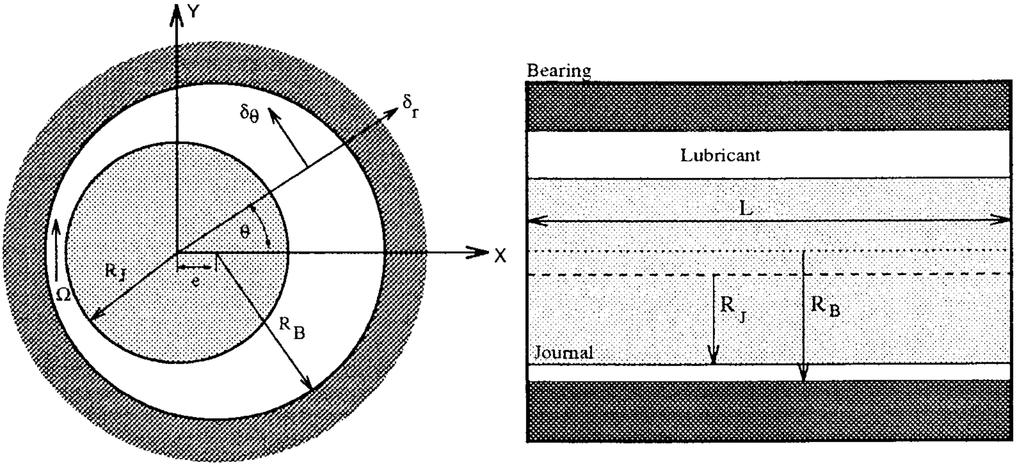

Figure 1. Geometry of the journal bearing model.

$$\tau_{xy} = \eta\left(\frac{\partial v}{\partial x} + \frac{\partial u}{\partial y}\right), \tag{2.9}$$

$$\tau_{yz} = \eta\left(\frac{\partial w}{\partial y} + \frac{\partial v}{\partial z}\right), \tag{2.10}$$

$$\tau_{xz} = \eta\left(\frac{\partial w}{\partial x} + \frac{\partial u}{\partial z}\right). \tag{2.11}$$

In this study the fluid density ρ is considered to be constant. In addition, the fluid is considered to be isotropic and isothermal. In the generalized Newtonian model the viscosity η depends on the local shear rate and pressure only. The formulation of the viscosity law will be discussed in the following section. The components (u, v, w) of the velocity field $\mathbf{u}$ are based on the Cartesian co-ordinates (x, y, z), and τ_{ij} $(i, j = x, y, z)$ are the components of the extra-stress tensor.

In the above system of equations u, v, w, p, $\tau_{i,j}$, $(i, j = x, y, z)$ are considered to be the dependent variables. If the stress components are eliminated from (2.2)–(2.4) using (2.6)–(2.11), we obtain a set of coupled non-linear partial differential equations involving only the velocity and pressure field. Generally $\mathbf{u}$ and p are known as the primary variables and $\boldsymbol{\tau}$ the auxiliary variable.

2.3. Viscosity

One of the most important physical properties of a lubricant is its viscosity. In fact, for a Newtonian liquid, it can be shown using the lubrication theory that the load carrying capacity is directly proportional to its viscosity. In normal usage, lubricants are exposed to a wide range of shear rate, temperature and pressure, and an important consideration is the dependence of viscosity on these three variables. To be acceptable, a lubricant must be able to function adequately over a wide range of temperature and pressure. The simplest viscosity model is the Newtonian model where the viscosity η is constant in the entire flow field. There are many non-Newtonian viscosity models which are used to model more complicated fluid behaviour such as shear-thinning, temperature-thinning, pressure-thickening and elasticity, as described in [3]. In the following we present a shear-thinning and pressure-thickening model only.

The Cross model [3] is most commonly used to model the shear-rate dependence of viscosity in the generalized Newtonian models. Therefore, the viscosity law we use has this dependence on shear-rate built into it. In addition, a dependence on pressure is introduced by using the Barus formulation. In practice, other models may also be included. The formulation of the fluid viscosity law [4] is given as follows:

$$\eta = \{\eta_\infty + (\eta_0 - \eta_\infty)[1 + (K_s\dot{\gamma})^m]^{-1}\} \times \exp\left(-\frac{\alpha}{3}\,\mathrm{trace}(\boldsymbol{\sigma}) + \frac{\beta}{\Theta}\right), \tag{2.12}$$

where the coefficient K_s, although independent of the shear rate $\dot{\gamma}$, is dependent on pressure and temperature. In particular, following [5], we choose

$$K_s = K_s(p) = \exp\left(-\frac{\bar{\alpha}}{3}\,\mathrm{trace}(\boldsymbol{\sigma}) + \frac{\bar{\beta}}{\Theta} + E\right), \tag{2.13}$$

and

$$\boldsymbol{\sigma} = -p\mathbf{I} + \mathbf{T}, \tag{2.14}$$

where $\boldsymbol{\sigma}$ is the total (Cauchy) stress tensor, $\mathbf{I}$ is the unit tensor and $\mathbf{T}$ is the extra-stress tensor defined as Equations (2.6)–(2.11). The constants η_0, η_∞, m, α, $\bar{\alpha}$, β, $\bar{\beta}$ and E are material parameters which must be estimated by best-fitting available experimental data and may be found in [4] and [5]. To represent isothermal flow the value of Θ in (2.13) and (2.14) is given a constant value which in this paper is $\Theta = 373.15$ K.

For 3D flow the explicit forms of trace($\boldsymbol{\sigma}$) and $\dot{\gamma}$ are given by

$$\mathrm{trace}(\boldsymbol{\sigma}) = \tau_{xx} + \tau_{yy} + \tau_{zz} - 3p, \tag{2.15}$$

and

$$\dot{\gamma}^2 = 2\left(\left(\frac{\partial u}{\partial x}\right)^2 + \left(\frac{\partial v}{\partial y}\right)^2 + \left(\frac{\partial w}{\partial z}\right)^2\right) + \left(\frac{\partial u}{\partial y} + \frac{\partial v}{\partial x}\right)^2 + \left(\frac{\partial u}{\partial z} + \frac{\partial w}{\partial x}\right)^2 + \left(\frac{\partial v}{\partial z} + \frac{\partial w}{\partial y}\right)^2. \tag{2.16}$$

2.4. *Initial and boundary conditions*

The above system of equations is to be solved subject to specified initial and boundary conditions. With reference to Figure 1, we can divide the boundary Γ into four parts:

$$\Gamma = \Gamma_J \cup \Gamma_B \cup \Gamma_C \cup \Gamma_L,$$

where Γ_J and Γ_B denote the surfaces of the journal and bearing respectively, and Γ_C and Γ_L denote the cross-sections of the bearing at $z = 0$ and $z = \pm L/2$ respectively. The velocity boundary conditions are

$$u(t) = u_J,\ v(t) = v_J,\ w(t) = 0, \quad \text{on } \Gamma_J, \tag{2.17}$$

$$u(t) = v(t) = w(t) = 0, \quad \text{on } \Gamma_B, \tag{2.18}$$

$\forall t > 0$. These represent no-slip and impermeability conditions on the journal and bearing surfaces.

We assume that the flow field in a finite bearing is symmetric about the middle of the bearing, Γ_C. Hence, u, v and p are symmetric functions of z and w is an antisymmetric function of z. Therefore, the boundary conditions on the centre plane are given by

$$w = 0,\ \frac{\partial u}{\partial z} = \frac{\partial v}{\partial z} = 0, \quad \text{on } \Gamma_C, \tag{2.19}$$

$$\frac{\partial p}{\partial z} = 0 \text{ on } \Gamma_C \tag{2.20}$$

Physically, the finite journal is open to the atmosphere at both ends so that

$$p = 0, \text{ on } \Gamma_L. \tag{2.21}$$

In real engine bearings, however, liquid film rupture due to a variety of causes prevents the formation of significant negative pressures. As a result, the region of positive pressure is usually limited in extent to roughly half the bearing. Oil holes and grooves further complicate the picture.

To fully define the problem it is sufficient to specify an initial state at time $t = 0$,

$$u(x, y, z, 0) = u_0, \qquad v(x, y, z, 0) = v_0, \qquad w(x, y, z, 0) = w_0. \tag{2.22}$$

In the numerical calculations care must be taken to avoid an impulsive start to the rotation of the journal, which can result in a large jump in pressure with an unrealistic increase in viscosity. The rotational speed of the journal should be increased smoothly from rest in which case (2.22) above needs to be modified.

3. THE SPECTRAL ELEMENT METHOD

In this study the spectral element method is chosen for the spatial discretization. In the spectral element method, a complex domain is decomposed into simpler domains called spectral elements, in each of which a spectral representation is used to represent each of the dependent variables. The solution is obtained using a discretization of the variational formulation of the problem in which the velocity components are assumed to be continuous across element boundaries. Spectral element methods were first presented in [6], and an excellent review is given in [7]. This method, like the spectral method, uses high-order polynomials as trial functions, and like the finite element method, decomposes the computational domain into a number of simpler domains on which local trial functions are defined. The hybrid character of the spectral element method enables it to overcome the shortcomings of both the spectral method and the finite element method but still retain their advantages. Since the trial functions of the spectral element method are local, the method can handle complex geometries easily. On the other hand, it is still a high-order weighted residual method, so the exponential convergence rate is achieved as the degree of the polynomial approximation in each element is increased. In the following sections a spectral element approach will be presented for the dynamically loaded journal bearing.

3.1. Variational formulation

In order to pose a weak formulation equivalent to the system of Equations (2.2)–(2.5), we first introduce the following function spaces:

$$V(\Omega) = \{(u, v, w) \in [H_0^1(\Omega)]^3\},$$

$$Q(\Omega) = \{p \in L^2(\Omega),\ p(x) = 0,\ \text{on}\ \Gamma_L\}.$$

where $H_0^1(\Omega)$ denotes the subspace of $H^1(\Omega)$ of functions which are zero on the boundary:

$$H^1(\Omega) = \{\phi \in L^2(\Omega);\ \nabla\phi \in [(L^2(\Omega))]^3\},$$

$$H_0^1(\Omega) = \{\phi \in H^1(\Omega);\ \phi = 0\ \text{on}\ \Gamma\},$$

where L_2 (Ω) is the space of square integrable functions.

For the sake of simplicity we choose, without loss of generality, the velocity field equal to zero on Γ. After multiplying (2.2)–(2.4) by the weighting function $(\bar{u}, \bar{v}, \bar{w}) \in V(\Omega)$ and (2.5) by $q \in Q(\Omega)$, and integrating by parts, we get the following variational formulation for (2.2)–(2.5) as: Find $(u, v, w) \in V(\Omega)$ and $p \in Q(\Omega)$ such that for $t \geq 0$

$$\rho \int_\Omega \frac{\partial u}{\partial t} \bar{u}\, \mathrm{d}\Omega + \rho \int_\Omega \left(u \frac{\partial u}{\partial x} + v \frac{\partial u}{\partial y} + w \frac{\partial u}{\partial z} \right) \bar{u}\, \mathrm{d}\Omega + \int_\Omega \frac{\partial \bar{u}}{\partial x} p\, \mathrm{d}\Omega + \int_\Omega \eta \left(\frac{\partial u}{\partial x}\frac{\partial \bar{u}}{\partial x} + \frac{\partial u}{\partial y}\frac{\partial \bar{u}}{\partial y} + \frac{\partial u}{\partial z}\frac{\partial \bar{u}}{\partial z} \right) \mathrm{d}\Omega = 0, \tag{3.1}$$

$$\rho \int_{\Omega} \frac{\partial v}{\partial t} \bar{v} \, d\Omega + \rho \int_{\Omega} \left(u \frac{\partial v}{\partial x} + v \frac{\partial v}{\partial y} + w \frac{\partial v}{\partial z} \right) \bar{v} \, d\Omega + \int_{\Omega} \frac{\partial \bar{v}}{\partial y} p \, d\Omega$$

$$+ \int_{\Omega} \eta \left(\frac{\partial v}{\partial x} \frac{\partial \bar{v}}{\partial x} + \frac{\partial v}{\partial y} \frac{\partial \bar{v}}{\partial y} + \frac{\partial v}{\partial z} \frac{\partial \bar{v}}{\partial z} \right) d\Omega = 0, \tag{3.2}$$

$$\rho \int_{\Omega} \frac{\partial w}{\partial t} \bar{w} \, d\Omega + \rho \int_{\Omega} \left(u \frac{\partial w}{\partial x} + v \frac{\partial w}{\partial y} + w \frac{\partial w}{\partial z} \right) \bar{w} \, d\Omega + \int_{\Omega} \frac{\partial \bar{w}}{\partial z} p \, d\Omega$$

$$+ \int_{\Omega} \eta \left(\frac{\partial w}{\partial x} \frac{\partial \bar{w}}{\partial x} + \frac{\partial w}{\partial y} \frac{\partial \bar{w}}{\partial y} + \frac{\partial w}{\partial z} \frac{\partial \bar{w}}{\partial z} \right) d\Omega = 0, \quad \forall (\bar{u}, \bar{v}, \bar{w}) \in V(\Omega), \tag{3.3}$$

and

$$\int_{\Omega} \left(\frac{\partial u}{\partial x} + \frac{\partial v}{\partial y} + \frac{\partial w}{\partial z} \right) \bar{p} \, d\Omega = 0, \quad \forall \bar{p} \in Q(\Omega). \tag{3.4}$$

Under certain conditions, one can prove that there exists an unique solution $(u, v, w) \in V(\Omega)$ and $p \in Q(\Omega)$ to the variational formulation (3.1)–(3.4) (see [8]). The task for this method is to find $(u, v, w) \in V(\Omega)$ and $p \in Q(\Omega)$ such that the residuals of the discretized form of the system (3.1)–(3.4) are minimized for all $(\bar{u}, \bar{v}, \bar{w}) \in V(\Omega)$ $\bar{p} \in Q(\Omega)$.

3.2. Local co-ordinate transformation

The spectral element method decomposes the computational domain Ω into K subdomains, say, denoted by Ω_k, $(k = 1, \ldots, K)$ such that

$$\Omega = \textstyle\bigcup_{k=1}^{k} \Omega_k, \quad \forall k, l, \ k \neq l, \ \Omega_k \cap \Omega_l = \emptyset. \tag{3.5}$$

With the above decomposition of Ω the variational formulation of system (3.1)–(3.4) can be written as

$$\rho \sum_{k=1}^{K} \int_{\Omega} \frac{\partial u}{\partial t} \bar{u} \, d\Omega_k + \rho \sum_{k=1}^{K} \int_{\Omega_k} G(u) \bar{u} \, d\Omega_k + \sum_{k=1}^{K} \int_{\Omega_k} \frac{\partial \bar{u}}{\partial x} p \, d\Omega_k$$

$$+ \sum_{k=1}^{K} \int_{\Omega_k} \eta^k \left(\frac{\partial u}{\partial x} \frac{\partial \bar{u}}{\partial x} + \frac{\partial u}{\partial y} \frac{\partial \bar{u}}{\partial y} + \frac{\partial u}{\partial z} \frac{\partial \bar{u}}{\partial z} \right) d\Omega_k = 0, \tag{3.6}$$

$$\rho \sum_{k=1}^{K} \int_{\Omega_k} \frac{\partial v}{\partial t} \bar{v} \, d\Omega_k + \rho \sum_{k=1}^{K} \int_{\Omega_k} G(v) \bar{v} \, d\Omega_k + \sum_{k=1}^{K} \int_{\Omega_k} \frac{\partial \bar{v}}{\partial y} p \, d\Omega_k$$

$$+ \sum_{k=1}^{K} \int_{\Omega_k} \eta^k \left(\frac{\partial v}{\partial x} \frac{\partial \bar{v}}{\partial x} + \frac{\partial v}{\partial y} \frac{\partial \bar{v}}{\partial y} + \frac{\partial v}{\partial z} \frac{\partial \bar{v}}{\partial z} \right) d\Omega_k = 0, \tag{3.7}$$

$$\rho \sum_{k=1}^{K} \int_{\Omega_k} \frac{\partial w}{\partial t} \bar{w} \, d\Omega_k + \rho \sum_{k=1}^{K} \int_{\Omega_k} G(w) \bar{w} \, d\Omega_k + \sum_{k=1}^{K} \int_{\Omega_k} \frac{\partial \bar{w}}{\partial z} p \, d\Omega_k$$

$$+ \sum_{k=1}^{K} \int_{\Omega_k} \eta^k \left(\frac{\partial w}{\partial x} \frac{\partial \bar{w}}{\partial x} + \frac{\partial w}{\partial y} \frac{\partial \bar{w}}{\partial y} + \frac{\partial w}{\partial z} \frac{\partial \bar{w}}{\partial z} \right) d\Omega_k = 0, \quad \forall (\bar{u}, \bar{v}, \bar{w}) \in V(\Omega_k) \tag{3.8}$$

and

$$\sum_{k=1}^{K} \int_{\Omega_k} \left(\frac{\partial u}{\partial x} + \frac{\partial v}{\partial y} + \frac{\partial w}{\partial z} \right) \bar{p} \, d\Omega_k = 0, \quad \forall \bar{p} \in Q(\Omega_k), \tag{3.9}$$

where $G(\cdot)$ is a convective operator and is defined as

$$G(\cdot) = u\frac{\partial}{\partial x} + v\frac{\partial}{\partial y} + w\frac{\partial}{\partial z},$$

and $V(\Omega_k)$ and $Q(\Omega_k)$ denote corresponding local spaces of functions in $V(\Omega)$ and $Q(\Omega)$ respectively, restricted to Ω_k.

Although the domain Ω may appear quite complicated, there are techniques which can be used to map each element Ω_k onto a parent element [9]. Let $\mathscr{F}$ be a continuous one-to-one mapping such that $\mathscr{F}(\Omega) = \hat{\Omega}$. Then under the mapping $\mathscr{F}$, there is a corresponding domain decomposition on $\hat{\Omega}$ and its subdomains $\hat{\Omega}_k$ also satisfy the connection property (3.5). For simplicity, here $\hat{\Omega}_k$ are assumed to be rectangular subdomains, which can be achieved by properly choosing $\mathscr{F}$. For each rectangular subdomain $\hat{\Omega}_k$ we can define a mapping from $\hat{\Omega}_k = [a_l^k, a_r^k] \times [b_l^k, b_r^k] \times [c_l^k, c_r^k]$ to $\aleph^3 = [-1, 1]^3$, by:

$$\xi = \frac{2}{|a_r^k - a_l^k|}(\hat{x} - a_l^k) - 1, \quad k = 1, 2, \ldots, K,$$

$$\zeta = \frac{2}{|b_r^k - b_l^k|}(\hat{y} - b_l^k) - 1, \quad k = 1, 2, \ldots, K,$$

$$\chi = \frac{2}{|c_r^k - c_l^k|}(\hat{z} - c_l^k) - 1, \quad k = 1, 2, \ldots, K.$$

where $(\hat{x}, \hat{y}, \hat{z})$ are the co-ordinates of a point in $\hat{\Omega}_k$ and (ξ, ζ, χ) are the corresponding local co-ordinates in $\aleph^3$, which is called the parent element or volume.

In fact, the image domain $\hat{\Omega}$ is more of a convenient mathematical concept than a computational necessity. In actual applications, the mapping can be carried out directly from Ω_k to the parent element $\aleph^3$. For the technical details of the implementation of the grid generation, the reader is referred to Reference [10] for the 2D case.

3.3. Basis

In order to set up the spectral element discretization, it is necessary to choose a simple basis to span a proper functional space for the Galerkin numerical approximation. In the present work, we will use the Gauss–Lobatto Legendre polynomials as a basis for the approximation space:

$$h_i(\xi) = -\frac{(1-\xi^2)L_N'(\xi)}{N(N+1)L_N(\xi_i)(\xi - \xi_i)}, \quad i = 0, 1, \ldots, N, \tag{3.10}$$

where L_N is the Nth-order Legendre polynomial, L_N' is the first-order derivative and the collocation points, ξ_i, are given by

$$-1 = \xi_0 < \xi_1 < \cdots < \xi_N = 1, \quad \forall i \in \{1, \ldots, N-1\}, \quad L_N'(\xi_i) = 0. \tag{3.11}$$

From the definition of $h_i(\xi)$, we obtain

$$h_i(\xi_j) = \delta_{ij}, \quad \forall i, j \in \{0, \ldots, N\},$$

where δ_{ij} is the Kronecker-delta symbol. There also exists a unique set of positive real number ρ_i, corresponding to ξ_i, $(0 \le i \le N)$, such that the integration rule

$$\int_{-1}^{1} \psi(x)\,\mathrm{d}x = \sum_{i=0}^{N} \rho_i\,\psi(\xi_i), \tag{3.12}$$

is exact for all polynomials $\psi(x)$ of degree $\leq(2N-1)$ on the interval $[-1, 1]$. Note that one advantage of using the Gauss–Lobatto Legendre polynomials as basis functions is that we only have to deal with one set of grid points for interpolation and numerical quadrature.

Then on the parent element, $\aleph^3$, we define a basis set $\{\phi_{ijl}\}$ as

$$\phi_{ijl}(\xi, \zeta, \chi)=h_i(\xi)h_j(\zeta)h_l(\chi), \quad i, j, l\in\{0, \ldots, N\}^3.$$

Note that we have chosen the resolution in the three spatial directions to be the same; however, in practice, this need not be the case. Now the basis set $\{\phi_{ijl}\}$ on the parent element $\aleph^3$ has its projection $\{\phi^k_{ijl}\}$ on each subdomain Ω_k through a mapping $\mathscr{F}$ and

$$\phi^k_{ijl}((x, y, z)|(x, y, z)\in\Omega_k)=h_i(\xi(x, y, z))h_j(\zeta(x, y, z))h_l(\chi(x, y, z)),$$
$$i, j, l\in\{0, 1, \ldots, N\}^3. \tag{3.13}$$

With well-distributed interpolation points on Ω_k, it can be proved that $\{\phi_{ijl}\}$ is complete (when $N\rightarrow\infty$) and orthogonal. Therefore, if V^h_k is the subspace spanned by $\{\phi^k_{ijl}\}\in V(\Omega_k)$, then there is a projection Π_k such that for any $u^k(x, y, z|(x, y, z)\in\Omega_k)\in V(\Omega_k)$

$$\Pi_k(u^k(x, y, z))=u^k_h(\xi(x, y, z), \zeta(x, y, z), \chi(x, y, z))\in V^h_k, \tag{3.14}$$

where u^k_h is the numerical approximation of $u^k\in V(\Omega_k)$. Then it follows that there is a projection Π such that for any $u(x, y, z|(x, y, z)\in\Omega)\in V(\Omega)$

$$\Pi(u(x, y, z))=u_h=\bigcup_{k=1}^{K} u^k_h(\xi(x, y, z), \zeta(x, y, z), \chi(x, y, z))\in\bigcup_{k=1}^{K} V^h_k, \tag{3.15}$$

where u_h is the numerical approximation of u by piecewise polynomials. The discretization parameter h is thus characterized by two numbers, the number of elements, K, and the polynomial degree within each element, N. Under proper conditions, one can construct convergent sequences of solution to (3.15) such that

$$\bigcup_{k=1}^{K} u^k_h\rightarrow u, \text{ as } N\rightarrow\infty \text{ or } \Delta_{\max}\rightarrow 0, \tag{3.16}$$

where $\Delta_{\max}$ is the maximum size of the subdomains Ω_k.

Now we can see that the spectral element method has two ways to achieve better numerical precision, i.e. by increasing the dimensions of the subspaces, N^3, and/or the number of the elements, K. Therefore, the method is flexible and the optimum choice for these two parameters depends on each individual problem to be solved. The flexibility of the spectral element method is one of its most attractive features compared with the spectral and finite element methods.

3.4. The spatial discrete formulation

Let us denote by $\mathscr{P}_{N,K}$ the space of all polynomials of degree N or less defined over each parent element $\aleph^3$, and V_h and Q_h the discrete spaces respectively, for the velocities and pressure, where for each h, $V_h\subset V(\Omega)$ and $Q_h\subset Q(\Omega)$ are compatible subspaces of $V(\Omega)$ and $Q(\Omega)$. Choosing the velocity field in $V_h=H^1_0(\Omega)\mathscr{P}_{N,K}$ and constructing a Gauss–Lobatto Legendre grid in the parent element $\aleph^3$, we expand the velocity field in tensor product form:

$$\mathbf{v}^k_h(\xi, \zeta, \chi)=\sum_{i=0}^{N_\xi}\sum_{j=0}^{N_\zeta}\sum_{l=0}^{N_\chi}\mathbf{v}^k_{ijl}\,\phi_{ijl}(\xi, \zeta, \chi)=\sum_{i=0}^{N_\xi}\sum_{j=0}^{N_\zeta}\sum_{l=0}^{N_\chi}\mathbf{v}^k_{ijl}\,h_i(\xi)h_j(\zeta)h_l(\chi),$$
$$(x, y, z)\in\Omega_k\rightarrow(\xi, \zeta, \chi)\in\aleph^3, \tag{3.17}$$

where $\mathbf{v}^k_{ijl} = \mathbf{v}_h(\xi^k_i, \zeta^k_j, \chi^k_l) = (u(\xi^k_i, \zeta^k_j, \chi^k_l), v(\xi^k_i, \zeta^k_j, \chi^k_l), w(\xi^k_i, \zeta^k_j, \chi^k_l))^T$ is the velocity at the tensor product Gauss–Lobatto Legendre point $(\xi^k_i, \zeta^k_j, \chi^k_l)$ in subdomain Ω_k, and the basis functions h_i, h_j and h_l are defined as in (3.10). Here N_ξ, N_ζ and N_χ are the numbers of collocation points in the three spatial directions respectively.

As for the finite element method, the velocity and pressure spaces must satisfy the Babuška–Brezzi inf-sup compatibility condition in order to have a solvable system leading to a pressure field that is not polluted by spurious pressure wiggles. In the framework of the spectral element method, Maday and Patera [7] have shown that a suitable choice for the pressure approximation space is

$$Q_h = L^2(\Omega)\mathscr{P}_{N-2,K}.$$

With this choice for the pressure approximation space the compatibility condition is satisfied. Therefore, we choose the pressure nodes to be the interior Gauss–Lobatto Legendre points. Thus the pressure approximation is given by

$$p^k_h(\xi, \zeta, \chi) = \sum_{i=1}^{N_\xi - 1} \sum_{j=1}^{N_\zeta - 1} \sum_{l=1}^{N_\chi - 1} p^k_{ijl}\, \tilde{\phi}_{ijl}(\xi, \zeta, \chi) = \sum_{i=1}^{N_\xi - 1} \sum_{j=1}^{N_\zeta - 1} \sum_{l=1}^{N_\chi - 1} p^k_{ijl}\, \tilde{h}_i(\xi)\tilde{h}_j(\zeta)\tilde{h}_l(\chi),$$
$$(x, y, z)\in\Omega_k \to (\xi, \zeta, \chi)\in\aleph^3, \tag{3.18}$$

where $\tilde{h}_i(\cdot)$ is defined as

$$\tilde{h}_i(\xi) = -\frac{(1-\xi^2_i)L'_N(\xi)}{N(N+1)L_N(\xi_i)\,(\xi - \xi_i)}. \tag{3.19}$$

Since the test functions $\bar{u}$, $\bar{v}$, $\bar{w}$ and $\bar{p}$ are arbitrary, we can choose appropriate test functions $\bar{u}$, $\bar{v}$, $\bar{w} \in V_h$, which are unity at a single point (ξ_i, ζ_j, χ_l) and zero at all other Gauss–Lobatto Legendre points and test function $\bar{p} \in Q_h$, which are unity at a single point (ξ_i, ζ_j, χ_l) and zero at all other interior Gauss–Lobatto Legendre points. By substituting the velocity and pressure expansions into the variational form (3.6)–(3.9), we can derive the following semi-discretized (discrete in space) statement of the 3D problem,

$$\rho \sum_{k=1}^{K} \frac{\mathrm{d}u^k_{ijl}(t)}{\mathrm{d}t} B^k_{ijl\alpha\beta\gamma} = -\sum_{k=1}^{K} (\eta^k u^k_{ijl} A^k_{ijl\alpha\beta\gamma} + \rho G^k_{ijl}(u) B^k_{ijl\alpha\beta\gamma} - p^k_{rst} D^k_{rst\alpha\beta\gamma}(u)), \tag{3.20}$$

$$\rho \sum_{k=1}^{K} \frac{\mathrm{d}v^k_{ijl}(t)}{\mathrm{d}t} B^k_{ijl\alpha\beta\gamma} = -\sum_{k=1}^{K} (\eta^k v^k_{ijl} A^k_{ijl\alpha\beta\gamma} + \rho G^k_{ijl}(v) B^k_{ijl\alpha\beta\gamma} - p^k_{rst} D^k_{rst\alpha\beta\gamma}(v)), \tag{3.21}$$

$$\rho \sum_{k=1}^{K} \frac{\mathrm{d}w^k_{ijl}(t)}{\mathrm{d}t} B^k_{ijl\alpha\beta\gamma} = -\sum_{k=1}^{K} (\eta^k w^k_{ijl} A^k_{ijl\alpha\beta\gamma} + \rho G^k_{ijl}(w) B^k_{ijl\alpha\beta\gamma} - p^k_{rst} D^k_{rst\alpha\beta\gamma}(w)), \tag{3.22}$$

$$\sum_{k=1}^{K} (u^k_{ijl} D^k_{ijlrst}(u) + v^k_{ijl} D^k_{ijlrst}(v) + w^k_{ijlrst}(w)) = 0, \tag{3.23}$$

where $A^k_{ijl\alpha\beta\gamma}$, $B^k_{ijl\alpha\beta\gamma}$, $D^k_{rst\alpha\beta\gamma}(\cdot)$ and $G^k_{ijl}(\cdot)$ are given in Appendix A. Once all the integrations have been computed for all elements, the contributions from neighbouring elements are summed along element interfaces. In this way we arrive at the following matrix statement of Equations (3.20)–(3.23):

$$\rho[B]\left[\frac{\mathrm{d}u(t)}{\mathrm{d}t}\right] = -\{\eta[A][u] + \rho[B][G(u)] - [D^T(u)][p] - [f(u)]\}, \tag{3.24}$$

$$\rho[B]\left[\frac{\mathrm{d}v(t)}{\mathrm{d}t}\right] = -\{\eta[A][v] + \rho[B][G(v)] - [D^T(v)][p] - [f(v)]\}, \tag{3.25}$$

$$\rho[B]\left[\frac{\mathrm{d}w(t)}{\mathrm{d}t}\right] = -\{\eta[A][w] + \rho[B][G(w)] - [D^T(w)][p] - [f(w)]\}, \tag{3.26}$$

$$[D(u)][u] + [D(v)][v] + [D(w)][w] = 0, \tag{3.27}$$

where $[u]$, $[v]$, $[w]$, $[G(\cdot)]$ and $[p]$ are the vectors whose components are the values of these functions at all collocation points (the Gauss–Lobatto nodes); $[f(\cdot)]$ are essential boundary conditions appearing in (2.17)–(2.21); the superscript T denotes transpose; and the global stiff matrices $[A]$, $[B]$ and $[D(\cdot)]$ are obtained by the summation of the local stiff matrices A^k, B^k, D^k, in the following format:

$$[C] = \sum_{k=1}^{K}{}' C^k. \tag{3.28}$$

Here Σ' denotes elemental direct stiffness summation, in which the continuity and boundary conditions imposed on u, v, w and p (Equations (2.17)–(2.21) respectively) are taken into account, i.e. rows and columns corresponding to the same global degree of freedom are summed, and rows and columns corresponding to essential boundary conditions are eliminated.

3.5. The temporal discrete formulation

We now discuss the temporal discretisation for the system (3.24)–(3.27). Since we consider the dynamically loaded journal bearing problem, the restriction on the time step for an explicit time marching method can be severe when the journal is tracked in time. In general, we may improve this situation by treating the non-linear operators explicitly and the linear operators implicitly. Here, the first-order backward Euler time marching scheme is used for the system (3.24)–(3.27):

$$\rho[B]\left[\frac{u^{n+1} - u^n}{\Delta t}\right] = -\{\eta[A][u^{n+1}] + \rho[B][G(u^n)] - [D^T(u)][p^{n+1}] - [f^n(u)]\}, \tag{3.29}$$

$$\rho[B]\left[\frac{v^{n+1} - v^n}{\Delta t}\right] = -\{\eta[A][v^{n+1}] + \rho[B][G(v^n)] - [D^T(v)][p^{n+1}] - [f^n(v)]\}, \tag{3.30}$$

$$\rho[B]\left[\frac{w^{n+1} - w^n}{\Delta t}\right] = -\{\eta[A][w^{n+1}] + \rho[B][G(w^n)] - [D^T(w)][p^{n+1}] - [f^n(w)]\}, \tag{3.31}$$

$$[D(u)][u^{n+1}] + [D(v)][v^{n+1}] + [D(w)][w^{n+1}] = [0], \tag{3.32}$$

in which $[u^n]$ represents an approximation of $[u(n\Delta t)]$, etc. and Δt is the time step. The implicit/linear and explicit/non-linear splitting techniques in the scheme (3.29)–(3.31) are motivated by the fact that in the full explicit treatment of the system (3.1)–(3.4) it is typically the second-order viscous operator that results in the most stringent time step restriction. Since the discrete equations associated with this operator can be efficiently and robustly inverted, it is clear that these terms should be treated implicitly. On the other hand, the non-linear inertia terms are both less restrictive in terms of time step and more difficult to invert than the viscous terms, and are, therefore, more conveniently treated in an explicit fashion. For notational purpose the Equations (3.29)–(3.32) can be reduced to a standard matrix form:

$$\eta[A][u^{n+1}] + \sigma[B][u^{n+1}] - [D^T(u)][p^{n+1}] = [F^n(u)], \tag{3.33}$$

$$\eta[A][v^{n+1}] + \sigma[B][v^{n+1}] - [D^T(v)][p^{n+1}] = [F^n(v)], \tag{3.34}$$

$$\eta[A][w^{n+1}] + \sigma[B][w^{n+1}] - [D^T(w)][p^{n+1}] = [F^n(w)], \tag{3.35}$$

$$[D(u)][u^{n+1}] + [D(v)][v^{n+1}] + [D(w)][w^{n+1}] = [0], \tag{3.36}$$

where $\sigma = \rho/\Delta t$ and $F^n(\cdot)]$ are defined as

$$[F^n(u)] = \sigma[B][u^n] - \rho[B][G(u^n)] + [f(u)],$$

$$[F^n(v)] = \sigma[B][v^n] - \rho[B][G(v^n)] + [f(v)],$$

$$[F^n(w)] = \sigma[B][w^n] - \rho[B][G(w^n)] + [f(w)].$$

It should be noted that the matrix $[A]$ is positive-definite and symmetric and $[B]$, the mass matrix, is diagonal due to the Gauss–Lobatto Legendre quadrature. Consequently, the absolute stability of Equations (3.33)–(3.36) is readily demonstrated by setting $[F^n(\cdot)] = [0]$ and multiplying all equations by $[u^{n+1}]$, $[v^{n+1}]$, $[w^{n+1}]$ and $[p^{n+1}]$ respectively, to arrive at

$$\|[u^{n+1}]\|_{0,h} < \|[u^n]\|_{0,h}, \qquad \|[v^{n+1}]\|_{0,h} < \|[v^n]\|_{0,h}, \qquad \|[w^{n+1}]\|_{0,h} < \|[w^n]\|_{0,h}. \tag{3.37}$$

Thus, the discrete Equations (3.33)–(3.36) are unconditionally stable. Here $\|\cdot\|_{0,h}$ denotes the discrete L^2-norm, $\|u\|_{0,h}((u, u))_h^{1/2}$. Further interesting results can be found in [7].

4. UZAWA METHOD

In this section, the Uzawa procedure will be used to decouple the pressure and velocity computations. In this way a saddle point problem will be replaced by two symmetric positive (semi)-definite systems.

We begin with a decoupling of the original problem (3.33)–(3.36) into two positive semi-definite symmetric forms, one for the velocities u, v, w and one for the pressure. First, for each of the velocity components u, v and w from the momentum equations (3.33)–(3.35), we formally solve

$$[u^{n+1}] = [H]^{-1}[D^T(u)][p^{n+1}] + [H]^{-1}[F^n(u)], \tag{4.1}$$

$$[v^{n+1}] = [H]^{-1}[D^T(v)][p^{n+1}] + [H]^{-1}[F^n(v)], \tag{4.2}$$

$$[w^{n+1}] = [H]^{-1}[D^T(w)][p^{n+1}] + [H]^{-1}[F^n(w)], \tag{4.3}$$

where $[H]$ is the discrete Helmholtz operator defined by

$$[H] = (\eta[A] + \sigma[B]).$$

We then insert (4.1)–(4.3) into the continuity equation (3.36) to obtain the following equation for the pressure:

$$\begin{aligned}&([D(u)][H]^{-1}[D^T(u)] + [D(v)][H]^{-1}[D^T(v)] + [D(w)][H]^{-1}[D^T(w)])[p^{n+1}]\\&\quad = [D(u)][H]^{-1}[F^n(u)] + [D(v)][H]^{-1}[F^n(v)] + [D(w)][H]^{-1}[F^n(w)].\end{aligned} \tag{4.4}$$

Thus the discrete problem (3.33)–(3.36) can be replaced with the discretely equivalent statement

$$[H][u^{n+1}] - [D^T(u)][p^{n+1}] = [F^n(u)], \tag{4.5}$$

$$[H][v^{n+1}] - [D^T(v)][p^{n+1}] = [F^n(v)], \tag{4.6}$$

$$[H][w^{n+1}] - [D^T(w)][p^{n+1}] = [F^n(w)], \tag{4.7}$$

$$[S][p^{n+1}] = [C], \tag{4.8}$$

where the discrete pressure matrix is

$$[S] = ([D(u)][H]^{-1}[D^T(u)] + [D(v)][H]^{-1}[D^T(v)] + [D(w)][H]^{-1}[D^T(w)]),$$

which is symmetric positive definite and

$$[C] = ([D(u)][H]^{-1}[F^n(u)] + [D(v)][H]^{-1}[F^n(v)] + [D(w)][H]^{-1}[F^n(w)]).$$

We make several observations about these systems. First of all, since the system matrices $[H]$ and $[S]$ are symmetric and positive (semi-)definite, standard elliptic solvers, such as the conjugate gradient iteration technique, can readily be applied. Secondly, since the pressure and velocity in Equations (4.5)–(4.8) are completely decoupled in the solution process, we can first solve equation (4.8) for the pressure p^{n+1} and then solve Equations (4.5)–(4.7) for each velocity component $(u^{n+1}, v^{n+1}, w^{n+1})$ with p^{n+1} known. Finally, the pressure operator $[S]$ is completely full due to the embedded inverse $[H]^{-1}$ and, therefore, a nested iterative approach is required to solve (4.8).

Using the Preconditioned Conjugate Gradient (PCG) method to solve this system is well documented in the literature (see [7]) and suitable preconditioners have been advocated which yield efficient numerical algorithms. However, for the solution of realistic journal bearing problems in which $c = R_B - R_J$ is very small and the eccentricity ratio c is near unity the system of equations is extremely ill-posed and the spectrum of $[S]$ is not so well-behaved (see [10]). In this situation, the standard choice of preconditioner for Equation (4.8) is not robust. Therefore, the construction of an effective preconditioner for such a system will be essential for the scheme to be efficient. In this paper, we use a preconditioner which changes dynamically in time, taking into account the current eccentricity ratio of the journal and the number of PCG iterations required for convergence at each time step. The preconditioner is based on the pressure matrix evaluated at a given eccentricity ratio. Then this preconditioner is used for the solution of the pressure problem at successive time steps for which, of course, the eccentricity ratio will be different from that of the preconditioner. The current preconditioner is changed when the number of iterations required for convergence of the outer conjugate gradient iteration exceeds a prescribed maximum number of iterations. A new preconditioner is then constructed corresponding to the current eccentricity ratio. The work involved in setting up a new preconditioner is negligible compared with the time taken to solve the full equations. This process continues until either a stable equilibrium point or closed orbit is found. Further details regarding the choice of preconditioner for this problem can be found in Reference [10].

5. MOTION OF THE JOURNAL

After performing an integration of the equations over one complete time step Δt, the reaction force F and torque C on the journal may be calculated as

$$\mathbf{F} = -\int_{\Gamma_J} \boldsymbol{\sigma} \cdot \mathbf{n} \, \mathrm{d}s, \tag{5.1}$$

$$C = -R_J \int_{\Gamma} \mathbf{n}^T \cdot \boldsymbol{\sigma} \cdot \mathbf{t} \, \mathrm{d}s, \tag{5.2}$$

where **n** and **t** are the unit vectors outward normal and tangential to the journal surface Γ_J. The reaction force is used to calculate the new position of the journal.

We assume that the centre of mass of the journal behaves as a particle of effective mass, M_e, situated at the centre of the journal. The equation of motion of the journal is then given by

$$M_e\ddot{\mathbf{r}} = \mathbf{F_a} + \mathbf{F}, \tag{5.3}$$

where **r** is the position vector of the centre of the journal with respect to a co-ordinate system fixed in space and $\mathbf{F_a}$ is the applied load, which, in this paper, is taken to be

$$\mathbf{F_a} = (0, F, 0), \qquad F = F_p \sin(\omega t) - M_e g + F_c, \tag{5.4}$$

where the parameters F_p and F_c allow one to specify the amplitude and mean level of the applied load.

The journal is tracked in time using a quasi-steady approximation for Equation (5.3). This is, at a given time $t = n\,\Delta t$, say, the steady flow equations are solved for the current position of the journal using the spectral element method. Since the quasi-steady approximation is used we do not have to take into account the speed of change of the mesh in the governing equations. The force which the fluid exerts on the journal is then calculated by integrating the normal stress around the journal. The right hand side of (5.3) is then updated and the equation is integrated in time using the forward Euler method to obtain the new position of the journal at time $t = (n+1)\,\Delta t$. The process is repeated by solving the steady flow equations in the new region between the journal and the bearing. Note that in this approximation the motion of the journal at successive time steps is treated explicitly and, therefore, the time step must satisfy the CFL condition. In general, the time step Δt can be chosen as follows: if E_r, E_a and E_z denote the number of spectral elements in the radial, azimuthal and axial directions respectively, and similarly, $N_r + 1$, $N_a + 1$ and $N_z + 1$ denote the number of Gauss–Lobatto nodes in those respective directions, the minimum inter-nodal distance is then

$$h_{\min} \approx \min\left\{\frac{c}{E_r N_r}, \frac{2\pi R_J}{E_a N_a}, \frac{L}{2E_z N_z}\right\}.$$

If U_T denotes the translational speed of the journal, then the CFL condition is

$$\Delta t \leq \frac{h_{\min}}{U_T}.$$

Now in a typical run, $U_T = O(1)$, while $h_{\min} = O(10^{-5})$, giving $\Delta t \leq 10^{-5}$.

6. STATICALLY LOADED JOURNAL BEARING

We first validate our 3D spectral element algorithm on the statically loaded journal bearing problem. In particular, we shall compare our 3D spectral element results for the static journal with both lubrication theory and the numerical results of Roberts *et al.* [11] which were obtained by using a spectral collocation approach.

6.1. Reynolds' equation

A statically loaded journal is, by definition, a journal which rotates about its own stationary axis. A full film Newtonian fluid will impart a load on a static journal in the direction orthogonal to the line joining the centres of the journal and the bearing. When the gap c is

Table I. Static results for $L/D = 1/10$

ε	SEM F_y	SEM C	SCM F_y	SCM C	SBT F_y	SBT C
0.70	0.11E0	0.54E−2	0.11E0	0.62E−2	0.18E0	0.53E−2
0.80	0.24E0	0.64E−2	0.24E0	0.62E−2	0.35E0	0.63E−2
0.90	0.80E0	0.89E−2	0.79E0	0.85E−2	0.10E1	0.88E−2
0.95	0.23E1	0.12E−1	0.23E1	0.12E−1	0.29E1	0.13E−1
0.99	0.17E2	0.30E−1	0.14E2	0.28E−1	0.33E2	0.33E−1

small compared with other dimensions, it is possible to perform an order of magnitude analysis on the full Navier–Stokes equation. This results in Reynolds' equation ([12]), which, in the absence of inertia, is

$$\frac{\partial}{\partial\theta}\left((1+\varepsilon\cos\theta)^3\frac{\partial p}{\partial\theta}\right)+\left(\frac{R}{2L}\right)^2\frac{\partial}{\partial z}\left((1+\varepsilon\cos\theta)^3\frac{\partial p}{\partial z}\right)=-6\eta\Omega R^2\frac{\varepsilon}{c^2}\sin\theta, \tag{6.1}$$

where Ω is the angular velocity of the journal and θ is the azimuthal angle as shown in Figure 1.

In many physical situations the long or short bearing approximations are valid. When either of these approximations is applied to the above equation a closed form expression for the pressure may be derived. The reaction force of the fluid on the journal (the load) is then calculated by integrating the pressure around the surface of the journal,

$$\mathbf{F}=\int_\Gamma p\mathbf{I}\cdot\mathbf{n}\,\mathrm{d}S. \tag{6.2}$$

Note that this expression differs from the one which we use (5.1) in that the extra-stress part of the Cauchy stress tensor is not included.

6.2. Long and short bearing approximation theories

The long bearing approximation assumes that the pressure field is constant along the z-direction and thus the effects of the side boundary conditions are negligible. When $\partial p/\partial z$ is neglected, the Reynolds' equation can be solved analytically to obtain the pressure,

$$p=p_0+\frac{6\eta\Omega R^2}{c^2}\frac{\varepsilon\sin\theta(2+\varepsilon\cos\theta)}{(2+\varepsilon^2)(1+\varepsilon\cos\theta)^2}. \tag{6.3}$$

Table II. Static results for $L/D = 1/1$

ε	SEM F_y	SEM C	SCM F_y	SCM C	LBT F_y	LBT C	SBT F_y	SBT C
0.70	0.81E2	0.64E−1	0.78E2	0.61E−1	0.22E3	0.84E−1	0.18E3	0.78E−1
0.80	0.12E3	0.82E−1	0.11E3	0.78E−1	0.28E3	0.11E0	0.35E3	0.12E0
0.90	0.22E3	0.13E0	0.21E3	0.12E0	0.41E3	0.16E0	0.10E4	0.27E0
0.95	0.35E3	0.19E0	0.33E3	0.18E0	0.59E3	0.23E0	0.29E4	0.68E0
0.99	0.90E3	0.44E0	0.82E3	0.42E0	0.13E4	0.53E0	0.33E5	0.68E1

Table III. Static results for $L/D = 10/1$

	SEM		SCM		LBT	
ε	F_y	C	F_y	C	F_y	C
0.70	0.21E4	0.82E0	0.20E4	0.79E0	0.22E4	0.84E0
0.80	0.27E4	0.11E1	0.26E4	0.10E1	0.28E4	0.11E1
0.90	0.40E4	0.16E1	0.38E4	0.15E1	0.41E4	0.16E1
0.95	0.56E4	0.23E1	0.55E4	0.23E1	0.59E4	0.23E1
0.99	0.13E5	0.51E1	0.13E5	0.50E1	0.13E5	0.53E1

Using (6.2), the force and torque for the long bearing are given by

$$F_y = \frac{12\pi\eta L\Omega R^3\varepsilon}{c^2\sqrt{(1-\varepsilon^2)(2+\varepsilon^2)}}, \tag{6.4}$$

and

$$C = \frac{2\pi L\Omega R^3}{c\sqrt{(1-\varepsilon^2)}} + \frac{F_y e}{2}. \tag{6.5}$$

The short bearing approximation assumes that the contribution of the side boundary conditions gives rise to a much larger pressure gradient than that due to the rotation of the journal. With $\partial p/\partial\theta$ neglected, the Reynolds' equation can again be solved analytically for the pressure, viz,

$$p = p_0 + \frac{3\eta\Omega\varepsilon\sin\theta}{c^2(1+\varepsilon\cos\theta)^3}\left(\frac{L^2}{4} - z^2\right). \tag{6.6}$$

Similarly, the force and torque for the short bearing are given by

$$F_y = \frac{\pi\eta L^3\Omega R\varepsilon}{2c^2(1-\varepsilon^2)^{3/2}}, \tag{6.7}$$

and

$$C = \frac{2\pi\eta L\Omega R^3}{c\sqrt{(1-\varepsilon^2)}} + \frac{F_y e}{2}. \tag{6.8}$$

6.3. Discussion of static results

Tables I, II and III give the values for the force component in the vertical direction, F_y and the torque C exerted by the fluid on the journal calculated in four different ways: (i) the 3D spectral element method (SEM) described in this paper; (ii) the 3D spectral collocation method (SCM) of [11]; (iii) the long bearing lubrication approximation theory (LBT); and (iv) the short bearing lubrication approximation theory (SBT). Tables I, II and III correspond to three different L/D ratios namely 0.1, 1.0 and 10. The spatial discretization parameters used for the SEM results in these tables are $(N_r, N_a, N_z\ E_r, E_a, E_z) = (4, 6, 4, 1, 6, 1)$ and is sufficient for spatially converged values of F_y and C. The corresponding physical parameters for the journal, bearing and the lubricant in these calculations are the same as those used in [11], i.e. given by Table IV with $\omega = 250$ rad/s.

Generally speaking, the spectral element solutions are almost identical with previous results of 3D Stokes solutions for all ratios of L/D, which validates our 3D spectral element algorithm. As expected the calculated force and torque are in agreement with long bearing lubrication approximation theory for $L/D = 10/1$ for all eccentricities. When $L/D = 1/10$ one would expect there to be agreement with the prediction of short bearing lubrication theory. The fact that there is not can be explained by the way the component of force F_y is calculated. In short bearing lubrication theory the contribution to the force of the extra-stress is omitted. This has negligible effect for $L/D = 10/1$, but has increasing influence for short bearings. If we neglect the contribution of the extra-stress in our computation of F_y when $L/D = 1/10$ we obtain agreement with short bearing theory. The comparison of the solutions for $L/D = 1/1$ is particularly interesting. One notes that the spectral element solution predicts less load capacity than either of the long and short bearing lubrication approximation solutions as $\varepsilon \leq 0.99$. The side leakage of the lubricant is permitted at both ends of the journal due to the variation of pressure in the axial direction for the spectral element solution in the case of the finite bearings. In this sense, at least, the behaviour of a finite bearing does not simply lie somewhere between the extremes predicted by the long and short bearing lubrication approximation theories.

7. DYNAMICALLY LOADED JOURNAL BEARING

A dynamically loaded journal bearing consists of a journal whose axis is not stationary but moves in response to forces imparted upon it. Such forces consist of the fluid's reaction force on the journal and also an applied load, such as the force of the piston in the case of a big-end journal bearing. Computationally, the dynamically loaded journal bearing presents a major computational challenge since the position of the journal needs to be tracked in time and a new mesh needs to be constructed at each time step.

7.1. Cavitation model

It has long been known that under many operating conditions a complete lubricating film is not maintained in a journal bearing. In such conditions the lubricant is unable to sustain the very low pressures that are generated within the journal bearing mechanism. The result of this is that the fluid ruptures and a cavitating region is formed. The occurrence of cavitation in journal bearings is shown to result in reduced power loss, bearing torque and load capacity. Dowson *et al.* [13], in an excellent review of cavitation, point out that cavitation need not have detrimental effects on the load carrying capacity of bearings. Although cavitation damage may occur in journal bearings there is significant evidence that cavitation may reduce wear by damping out self-excited instability that occurs in dynamically loaded journal bearings. This instability is known as whirl instability.

The suggestion that whirl instability occurs in the full-film dynamically loaded journal bearing (with zero applied load) has been made by many investigators. In such cases, the journal moves from an unstable equilibrium position and gradually tends towards the journal in an ever increasing whirling motion. The period of this orbit is twice that of the journal's

Table IV. The physical parameters for the journal bearing

Journal radius (R_J)	0.03125 m	Constant viscosity (η)	5×10^{-3} Pas
Bearing radius (R_B)	0.03129 m	Gravity acceleration (g)	10 m/s^2
Bearing length (L)	0.06250 m	Density (ρ)	820 kg/m^3

angular velocity about its own axis resulting in the term *half-speed whirl*. In this situation the bearing is deemed to have failed since the journal will eventually touch the bearing. In practice the full film condition is not realistic since in many journal bearing models the large negative pressures produced in the oil film cause the oil to vaporize leading to cavitation.

There are many ways of modelling cavitation for 2D journal bearings of which the half Sommerfeld (π-film) cavitation model is a notable example. In this model the cavitation region is assumed to occupy the divergent half of the region between the journal and the bearing. The lubricant is assumed to occupy the convergent part of this region. Thus, for the purposes of calculating the force exerted on the journal by the fluid, the pressure boundary condition has been set

$$p = 0, \text{ at } \theta = 0; \text{ and } \pi < \theta < 2\pi.$$

If the short bearing approximation is used, a more sophisticated model is the oscillating π-film model. This allows the cavitating region to change dynamically in response to the behaviour of the journal. In this model the value of θ_1 is chosen to be the smallest value of $\theta > \pi$ for which $p = 0$ and the cavity is then assumed to occupy the region $\pi + \theta_1 < \theta < 2\pi + \theta_1$. There is documented evidence that this condition is a reasonable approximation to physical reality (see [12]). A useful comparison of the various boundary conditions used to describe cavitation models for the journal bearing can be found in [14].

However, in the case of the 3D journal bearing it is no longer necessary to specify *a priori* the position of the cavitation region. Since ambient pressure conditions are imposed at the ends of the journal bearing the pressure is determined uniquely. Therefore, unlike the corresponding situation in 2D the pressure level does not need to be set by specifying the pressure at a single point in the domain. In this paper two 3D cavitation models are presented. The first model is similar to the 2D single-phase cavitation model described in [14]. However, the 3D version of this model differs in that the arbitrariness of pressure is not addressed and no assumptions are made about the size of the cavitating region. In this approach the governing equations for the lubricant are solved subject to the full-film assumption and the cavitation region is then determined by the region of subambient pressures. We shall refer to this 3D single-phase cavitation model as model (A) for convenience.

The second model considered is the 3D *viscosity cavitation model*, so called since the cavitation region is related to the viscosity of the fluid. This idea was presented by Davies and Li [4] for statically loaded journal bearings and implemented for 2D dynamically loaded journal bearings by Gwynllyw *et al.* [2]. This model avoids the complex programming required to trace the moving boundary for the cavitation region, by incorporating a viscosity function for the lubricant which filters out the subambient pressures within the cavitation region. In this model we make no attempt at modelling rupture, and simply assume that there remains fluid in the cavitation region. In this region the viscosity function decreases quickly but smoothly to an asymptotic value $\eta_{\min}$. Ideally we would wish to choose $\eta_{\min}$ to be approximately the viscosity of air but such a small value leads to difficulties in the numerical convergence of the algorithm. A value of $\eta_{\min} = 4.0 \times 10^{-4}$ Pas has been used in our numerical calculations. We shall refer to this 3D *viscosity cavitation model* as model (B).

For both cavitation models the reaction forces are calculated by integrating the Cauchy stress tensor over the non-cavitating region. In the following section, we incorporate the above two cavitation models into our solution of the fully non-linear governing equations (2.2)–(2.12). We shall investigate whether cavitation in the 3D case has as significant an effect on the dynamics of the journal as reported for the 2D case by [14].

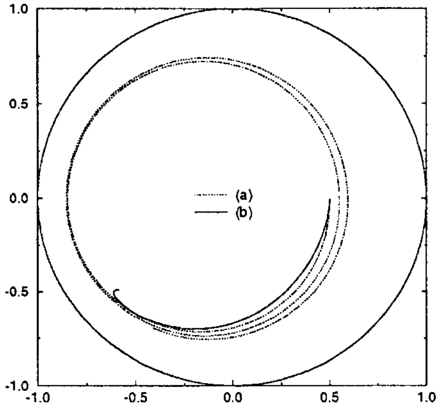

Figure 2. Comparison of trajectories for (a) full film model and (b) cavitation model (A) for a journal with a constant applied load, $M_e = 200$ kg, $\omega = 500$ rad/s, $L/D = 1/1$ and $F_c = 1.0 \times 10^4$ N starting from $(\varepsilon_0, \phi_0) = (0.5, -\pi)$.

7.2. Constant applied load

In this section we investigate the journal's motion when it is subject to a constant applied load $F_c \neq 0$ with $F_p = 0$. Comparison is made between the results obtained by assuming a full-film condition, the 3D single phase cavitation model (A) and the viscosity cavitation model (B). The geometric data and fluid parameters used in our numerical calculations are listed in Table IV, and correspond to an L/D ratio of 1/1 unless otherwise stated.

One of the main goals of this paper is to investigate the effects of a finite length on a journal bearing mechanism. This is done by comparing the dynamics of a finite length journal bearing with one of an infinite length (2D journal bearing). It has already been shown in [14] and [15] that, under the full film assumption, every trajectory of the 2D journal spirals towards the bearing and no stable equilibrium points or closed orbits are found. Cavitation in the 2D case is found to have significant stabilizing properties.

The first example is one in which the applied load is constant, $F_c = 1.0 \times 10^4$ N, with an effective mass $M_e = 200$ kg. The angular velocity of the journal is 500 rad/s. The journal is initially situated at $(\varepsilon_0, \phi_0) = (0.5, \pi)$, where ε_0 is the initial eccentricity ratio and ϕ_0 is the initial attitude angle. The results of the first example are illustrated in Figures 2–4. Figure 2 illustrates a comparison of the trajectories of the journal centre for the two models in the form of a clearance circle plot in which the bounding circle and its centre correspond to $\varepsilon = 1.0$ and $\varepsilon = 0.0$ respectively, whilst Figures 3 and 4 show the behaviour of the eccentricity ratio and the cosine attitude angle of the journal respectively, as a function of time.

For the full-film model the journal initially moves downwards owing to the constant applied load F_c and its weight $M_e g$, see curve (a) in Figure 2. However, as its eccentricity increases, the journal's rotation about its own axis becomes the dominating effect and the journal enters the half-speed whirl scenario whereby it gradually moves outwards in a whirling motion, the period of which is twice that of its own axial rotation. Figure 4 shows that the journal does enter half-speed whirl and thus as time increases further this path will approach $\varepsilon = 1.0$ and the journal will eventually touch the bearing.

It is clear from curve (b) in Figure 2 that the single-phase cavitation model has a significant stabilizing effect upon the journal in 3D. Such an effect also occurs in infinite length journal bearings [14,15]. Again the journal moves downwards as a result of the applied load F_c and its own weight $M_e g$, but this time its angular rotation spirals the journal inwards towards an

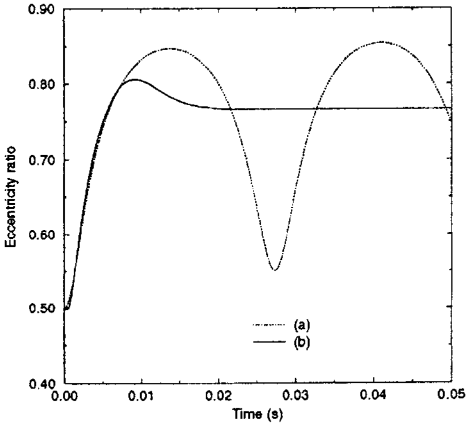

Figure 3. Evolution of the eccentricity ratio for the full film and cavitation (A) models. All parameters are the same as those in Figure 2.

equilibrium point, that is, the point at which the fluid's reaction force balance the journal's weight and the applied load. This demonstrates that the inclusion of a cavitation model in 3D journal bearings also has a stabilizing influence.

When an equilibrium point exists its position appears to be independent of the initial position of the journal for both 3D cavitation models employed in this study. An examination of this can be found in Figure 5, in which cavitation model (A) is used for a journal with two different initial positions, namely $(\varepsilon_0, \phi_0) = (0.75, 0)$ and $(0.5, -0.27)$. Both journals converge to the same equilibrium point $(\varepsilon, \phi) = (0.9, 1.05)$. Indeed, we found no case whereby a bifurcation in the equilibrium points exist. For both the long and short bearing limits of lubrication theory it can be shown that, with a π-film cavitation model, only one equilibrium point exists for the stability of the system.

Next we compare the trajectories generated by the two different cavitation models (A) and (B). The comparison is illustrated in Figure 6, in which the journal applied load is its own weight, that is, $W_e = M_e g = 4000$ kg and $F_c = 0$. The journal has angular velocity $\omega = 500$

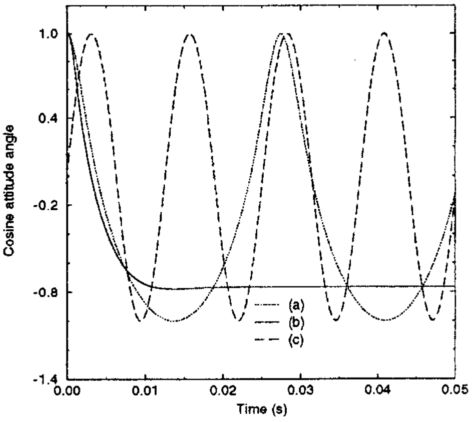

Figure 4. Cosine of the attitude angle as function of time for the two cases considered in Figure 2. Plots (a) and (b) give the results of the full film and cavitation (A) models respectively, together with (c) $\sin(\omega t)$ for reference with the journal angular velocity.

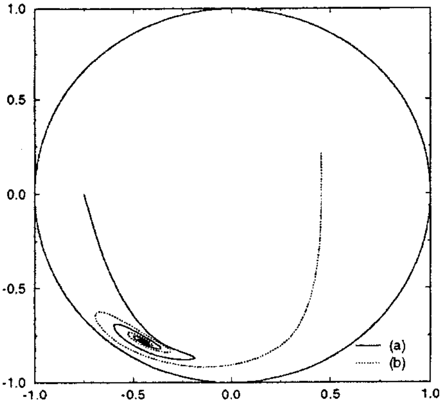

Figure 5. Comparison of trajectories for a journal starting from different positions with cavitation model (A) and a constant applied load $W_e = M_e g = 4.0 \times 10^4$ N and $L/D = 1/1$. Plots (a) and (b) show the journal starting points at $(\varepsilon_0, \phi_0) = (0.75, 0)$ and $(\varepsilon_0, \phi_0) = (0.5, -0.27)$ respectively.

rad/s. Stable paths are achieved for both cavitation models although the positions of the equilibrium points are different. The initial stages of these trajectories are shown in Figures 7 and 8. The two equilibrium points have the same eccentricity ratio ($\varepsilon = 0.9$) but differing attitude angles, $\phi = 1.05$ for model (A) and $\phi = 0.9$ for model (B). The fact that both models have the same equilibrium eccentricity ratio was also reported by Gwynllyw *et al.* [14] for their comparison of the 2D two-phase and 2D one-phase cavitation models. The result is that neither cavitation model seems to have a greater stabilizing effect when compared with the other. However, the position of the equilibrium point is sensitive to the choice of the cavitation models. We shall discuss this matter further for a variable applied load in the next section.

We consider the case of a journal with different magnitudes of constant applied loads using the cavitation model (A). In this example the journal has the angular velocity $\omega = 500$ rad/s with an effective mass $M_e = 200$ kg. We impose, respectively, two constant applied loads (a) $F_c = 5.0 \times 10^3$ N and (b) $F_c = 10^4$ N on the journal. The comparison of the trajectories corresponding to these two loads is shown in Figure 9. As expected, a larger load results in a

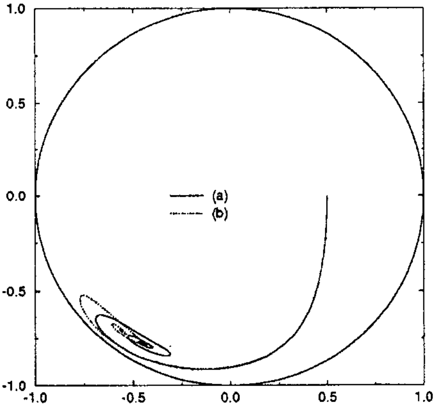

Figure 6. Comparison of trajectories of cavitation models (A) and (B) for a journal with $W_e = M_e g = 4.0 \times 10^4$ N, $\omega = 500$ rad/s. Plots (a) and (b) give the results of cavitation models (A) and (B) respectively.

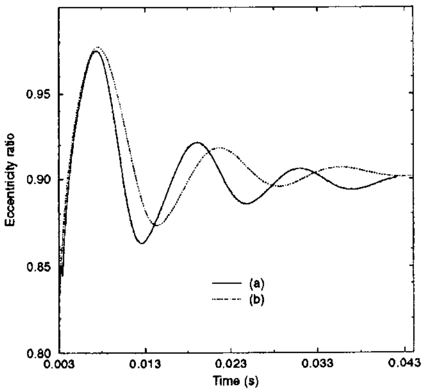

Figure 7. Eccentricity ratio versus time for the two cases considered in Figure 6. Plots (a) and (b) give the results of cavitation models (A) and (B) respectively.

larger eccentricity ratio and generates a smaller minimum oil film thickness whilst, a smaller load produces a larger one. This is seen in Figure 9. Although we found no significant difference in the shape of the two trajectories, since both journals approach equilibrium points at the end of a spiraling motion, there is a difference in locations of those points. This indicates that the position of an equilibrium point is determined by the magnitude of the constant applied load.

7.3. Variable applied load

Variable applied loads for the dynamically loaded journal bearings have been studied by many investigators using the short or long bearing approximations (see for example [15,16]). To the authors' knowledge, a few have used the full set of governing equations and studied the non-linear dynamics of the journal bearing under variable applied load conditions (see [14] for the 2D case). In this section we investigate the effect of variable applied loads on the journal orbits. Thus we have $F_p \neq 0$ in Equation (5.4) and set $F_c = 0$ for convenience.

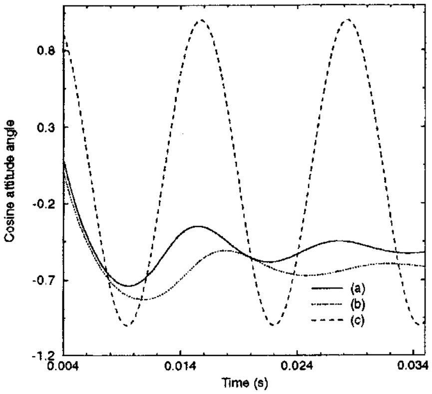

Figure 8. Cosine of the attitude angle versus time for the two cases considered in Figure 6. Plots (a) and (b) give the results of cavitation models (A) and (B) respectively, together with (c) $\sin(\omega t)$ for reference with the journal angular velocity.

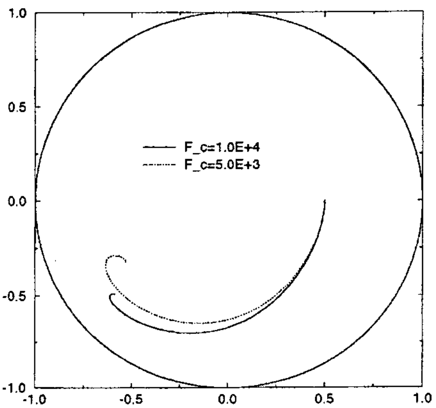

Figure 9. Comparison of the trajectories with different constant applied loads $F_c = 5.0 \times 10^3$ N and $F_c = 10^4$ N. Other parameters are $M_e = 200$ kg and $\omega = 500$ rad/s.

Under the full-film assumption, the variable applied load gave similar results to the constant applied load case in the sense that whirl instability eventually occurs. The variable applied load significantly alters the path initially but later, as the fluid's reaction force becomes dominant at higher eccentricities, the journal's path progressively resembles that encountered in whirl instability. The result, therefore, is bearing failure.

When cavitation is included in the finite length bearing the application of an applied load was found not to induce instability. That is, a system which was stable under a constant applied load ($F_p = 0$) was also found to be stable under a variable applied load ($F_p \neq 0$). Instead of an equilibrium point in the case of a constant applied load, the result with a variable applied load was a closed orbit with the same period as the applied load. These findings agree with the findings of Reference [14] for 2D bearings.

An example of the stable closed path is given in Figure 10, where cavitation model (A) has been employed and the magnitude of the variable applied load is $F_p = 5 \times 10^4$ N. The journal is seen to leave its initial position at $(\varepsilon_0, \phi_0) = (0.5, 0)$ and very quickly enters a closed path driven by the applied load and the reaction forces of the lubricant. Figures 11 and 12, respectively, illustrate the dependence of the eccentricity ratio and the attitude angle with time.

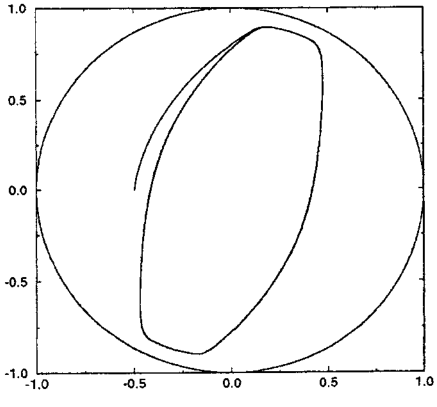

Figure 10. Trajectory of the journal centre for cavitation model (A) with a variable applied load $F_p = 5.0 \times 10^4$ N. Other parameters are $M_e = 200$ kg, $\omega = 250$ rad/s, and $(\varepsilon_0, \phi_0) = (0.5, 0)$.

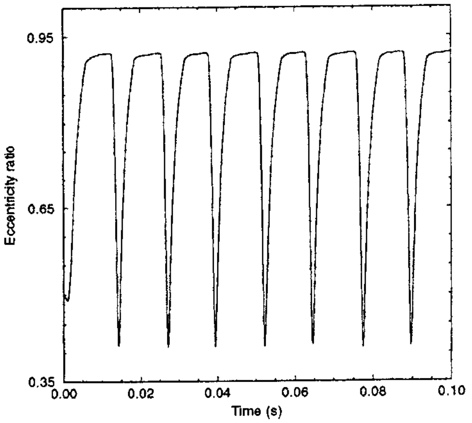

Figure 11. Evolution of the eccentricity ratio versus time for the case considered in Figure 10.

Referring to Figure 12 and comparing with the plot of sin(ωt) shows that the period of the closed path is the same as that of the applied load. Again, this shows that the applied load is dominant in determining the period of the path.

For the case of the variable applied load the locus of the closed path is independent of the initial position of the journal. Evidence to support this statement is provided in Figure 13 with the cavitation model (A). This is similar to the findings of the previous section where the equilibrium point is independent of the initial position of the journal. This evidence supports the claim that the final closed orbit for a given variable applied load (or the stable equilibrium position for a constant applied load) is independent of the initial condition, and is not confined to small initial displacements for a stable journal.

The effect of different magnitudes of variable applied loads is illustrated in Figure 14. These results are for cavitation model (A) with variable applied loads (a) $F_p = 5 \times 10^4$ N and (b) $F_p = 5 \times 10^3$ N. Unsurprisingly, decreasing the magnitude of F_p results in a larger minimum oil film thickness. There is significant difference as well in the shape of the closed path with the lower variable applied load giving a more rounded path. The comparison of the eccentricity ratios of the two paths is illustrated in Figure 15.

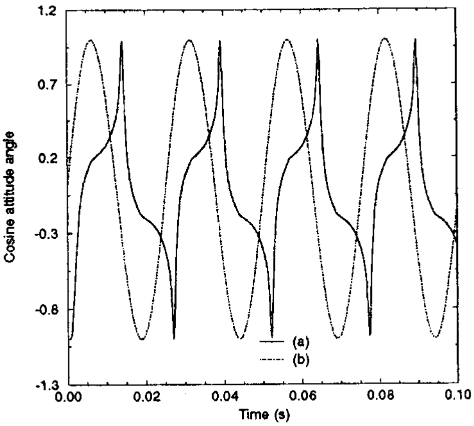

Figure 12. Cosine of the attitude angle (a) as a function of time for the case considered in Figure 10, together with (b) sin(ωt) for reference with the journal angular velocity.

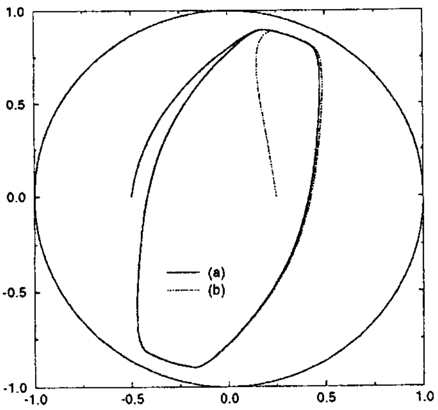

Figure 13. Comparison of trajectories for a journal starting from different positions (a) $(\varepsilon_0, \phi_0) = (0.5, 0.0)$ and (b) $(\varepsilon_0, \phi_0) = (0.25, \pi)$. Other parameters are $M_e = 200$ kg, $F_p = 5.0 \times 10^4$ N, $L/D = 1/1$ and $\omega = 250$ rad/s.

An important parameter in 3D journal bearings is the ratio of the length to the diameter of the journal L/D. Changing the length of the journal can have a significant effect on the journal's path as well as journal performance. We support this comment by comparing the two paths in Figure 16 where the larger path corresponds to a bearing whose length is one-tenth of that corresponding to the smaller path. Note that doubling the length of the journal does not mean *de facto* that the effective mass of the journal is doubled. The effective mass of the journal includes the mass of the whole crankshaft and not just that part enclosed in a supporting bearing (the journal). Although automotive engineers are constrained by the crankshaft in the design of engines they have freedom to play with the length of the main bearing. Therefore, the question as to how the length of the journal affects its path, keeping all other parameters constant, is an important one. With the same variable applied load F_p, we found that a decrease in the bearing's length always results in larger orbits, or equivalently, smaller minimum oil film thicknesses. Physically, this is not surprising. It is well known (see [12]) that for a given eccentricity ratio the fluid reaction force, per unit bearing length, exerted on a short bearing is many times less than that carried by a long bearing. Similarly, for a given

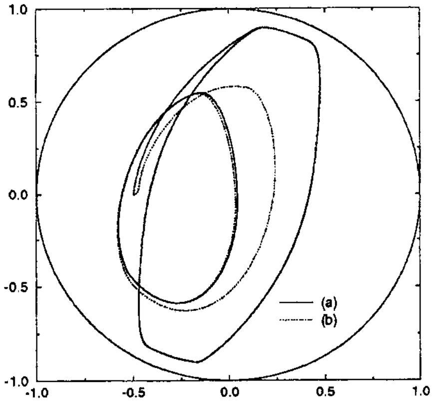

Figure 14. Comparison of trajectories for a journal having different magnitudes of applied loads (a) $F_p = 5 \times 10^4$ N and (b) $F_p = 5.0 \times 10^3$ N. Other parameters are $M_e = 200$ kg, $L/D = 1/1$ and $\omega = 250$ rad/s.

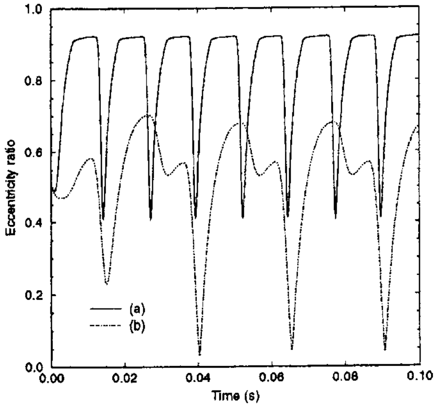

Figure 15. Comparison of eccentricity ratios versus time for the case considered in Figure 14.

value of an applied load, a shorter bearing results in a larger eccentricity ratio compared with a longer bearing. This effect is shown in Figure 17, where the eccentricity ratio when the journal reaches its equilibrium point is plotted as a function of the ratio L/D. It is seen that for a given constant applied load $F_c = 10^4$ N with $M_e = 200$ kg the dependence of eccentricity ratio on L/D is almost exponential corresponding to the relation

$$\varepsilon = a \exp\left(\frac{-bL}{D}\right).$$

The parameters a and b in this relationship depend on F_c. It is useful to have this formulation in the bearing operation [12]. In our example, these constants are $a = 0.975$ and $b = 0.198$ for the given applied load $F_c = 10^4$ N and $M_e = 200$ kg. Looking at the variation of the bearing load capacity with the ratio L/D in Table V, it is clear that the load bearing capacity is significantly reduced when the bearing length is decreased. In other words, the eccentricity ratio of the final equilibrium point is significantly increased if the bearing length is decreased. For example, we see in Table V, corresponding to the applied load 10^4 N, that $\varepsilon = 0.1105$ when $L/D = 10/1$, $\varepsilon = 0.6869$ when $L/D = 1/1$, and $\varepsilon = 0.92$ when $L/D = 1/2$. Moreover, when the

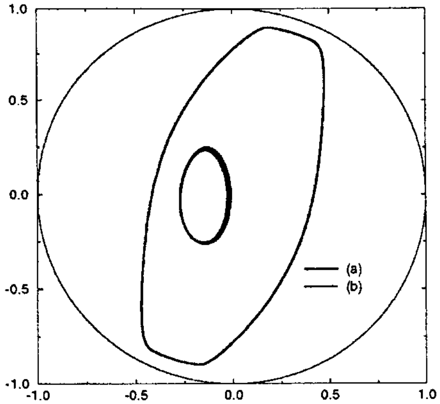

Figure 16. Comparison of trajectories for different bearing lengths (a) $L = 0.0625$ m and (b) $L = 0.625$ m, with $F_p = 5.0 \times 10^4$ N, $\omega = 250$ rad/s and the same journal radius.

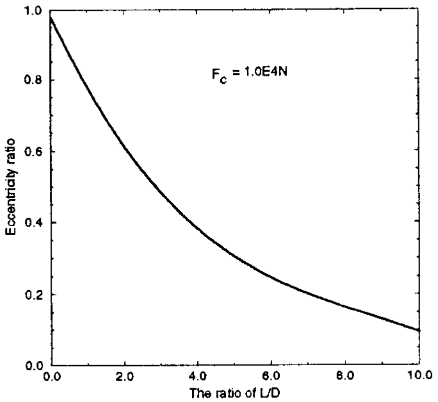

Figure 17. Eccentricity ratio versus the ratio of L/D for a fixed applied load $F_c = 10^4$ N.

applied load is 10^5 N, the final eccentricity ratio is $\varepsilon = 0.9223$ when $L/D = 1/1$, but when $L/D = 10/1$ it is only $\varepsilon = 0.4355$. When $L/D = 1/2$ the journal fails when the applied load is over 5.0×10^4 N for our example. This clearly demonstrates that the bearing length is an important parameter when determining the load bearing capacity contributing to either bearing failure or journal stability depending on its value.

Our last example demonstrates that distinct trajectories are generated for different cavitation models as was the case for a constant applied load. In this example, the journal has a variable applied load $F_p = 5.0 \times 10^4$ N. A comparison of the trajectories resulting from the two models (A) and (B) is shown in Figure 18. For each of the models a closed trajectory of the journal centre has been found. However, the closed path generated by model (B), compared with the path generated by model (A), is wider in the horizontal direction and narrower in the vertical direction. In particular, there is a significant difference in the maximum eccentricity ratio. This can be seen more clearly in Figure 19, where it is found that $\varepsilon_{\max} = 0.921$ for model (A), but $\varepsilon_{\max} = 0.91$ for model (B). Again, this example indicates that for a variable applied load the trajectory of the journal centre is also sensitive to the choice of the cavitation models.

In all our numerical calculations we found that the reaction force, which the lubricant exerts on the journal, is always comparable, in magnitude, with the applied load. Hence, the applied load is at least a contributory factor to the trajectory of the journal. Further, for all the stable trajectories generated the end effect was an equilibrium point in the case of a constant applied load and a closed path for the case of a variable applied load. We shall not fully address the question of whether the application of a non-zero F_p to a previously stable system always produces a closed path. Of course, there always exists a large enough F_p whereby the journal's

Table V. Dependence of eccentricity ratio at equilibrium point on F_c and L/D

Load	$L/D = 10/1$	$L/D = 1/1$	$L/D = 1/2$
1.0×10^3	—	—	0.7718
5.0×10^3	—	0.6232	0.8529
1.0×10^4	0.1105	0.6869	0.9201
5.0×10^4	0.2896	0.8149	>0.99
1.0×10^5	0.4355	0.9223	—
1.0×10^7	0.9575	>0.99	—

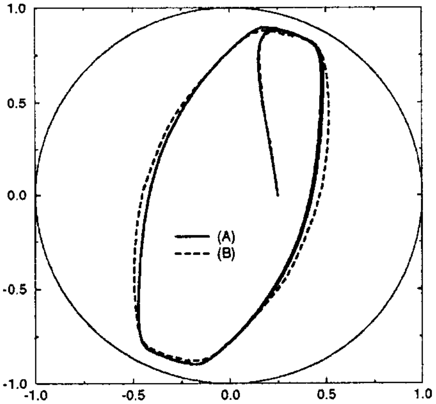

Figure 18. Comparison of trajectories for cavitation models (A) and (B). Here plots (a) and (b) correspond to models (A) and (B) respectively. The parameters used are $M_e = 200$ kg, with $F_p = 5.0 \times 10^4$ N and $\omega = 250$ rad/s.

eccentricity ratio exceeds our numerical tolerance of $\varepsilon = 0.99$ although this certainly does not mean that a theoretical limit cycle does not exist.

8. CONCLUDING REMARKS

In this paper a moving spectral element method has been presented for studying the effects of a non-Newtonian lubricant on the dynamics of a 3D journal bearing. The parameters in the fluid model have been obtained from experimental results on commercially manufactured lubricants. As for the corresponding 2D case we have shown that a constant viscosity lubricant results in bearing failure under all the conditions which have been tested. Cavitation has been modelled in two ways. First, by using the full-film assumption and then calculating the force on the journal by ignoring the region of subambient pressures. Secondly, by using a viscosity cut-off function that quickly but smoothly reduces the viscosity to some small value when the pressure in the lubricant is subambient. The inclusion of a model for cavitation is shown to

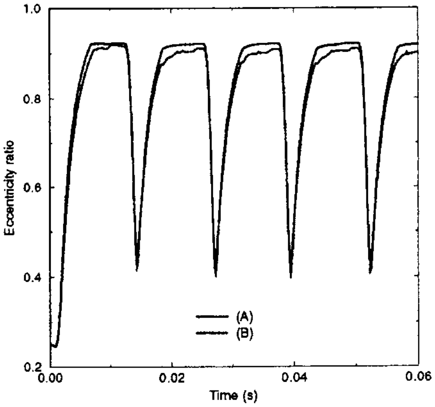

Figure 19. Eccentricity ratio versus time for the two cases considered in Figure 18. Plots (a) and (b) show the results of cavitation models (A) and (B) respectively.

stabilize the motion of the journal with the result that for a constant applied load the journal can reach an equilibrium point and for a variable applied load the journal can reach a closed path. The final path of the journal depends on the magnitudes and frequency of the applied loads, but not on the initial position of the journal.

More significantly, however, the effect of 3D on the dynamics of the journal bearing has been demonstrated by varying the ratio L/D and results presented showing the differences in the paths keeping all other parameters the same.

ACKNOWLEDGMENTS

This work was supported by Shell Research Ltd., Thornton Research Centre, Cheshire, UK. We wish to thank Professor K. Walters and Dr. G.W. Roberts of the University of Wales for many fruitful discussions. XKL gratefully acknowledges the support of the School of Computing Sciences, De Montfort University, Leicester.

APPENDIX A. FORMULATIONS OF A, B, D, G

The expressions defining A, B, D and G are:

$$\begin{aligned} A^k_{ijl\alpha\beta\gamma} = \int_{\aleph^3} \Bigg(& \frac{\partial\phi^k_{ijl}(\xi, \zeta, \chi)}{\partial x}\frac{\partial\phi^k_{\alpha\beta\gamma}(\xi, \zeta, \chi)}{\partial x} + \frac{\partial\phi^k_{ijl}(\xi, \zeta, \chi)}{\partial y}\frac{\partial\phi^k_{\alpha\beta\gamma}(\xi, \zeta, \chi)}{\partial y} \\ & + \frac{\partial\phi^k_{ijl}(\xi, \zeta, \chi)}{\partial z}\frac{\partial\phi^k_{\alpha\beta\gamma}(\xi, \zeta, \chi)}{\partial z}\Bigg)\left|J^k(\xi, \zeta, \chi)\right| \, \mathrm{d}\xi \, \mathrm{d}\zeta \, \mathrm{d}\chi, \end{aligned} \tag{A1}$$

$$B^k_{ijl\alpha\beta\gamma} = \int_{\aleph^3} \phi^k_{ijl}(\xi, \zeta, \chi)\phi^k_{\alpha\beta\gamma}(\xi, \zeta, \chi)\left|J^k(\xi, \zeta, \chi)\right| \, \mathrm{d}\xi \, \mathrm{d}\zeta \, \mathrm{d}\chi, \tag{A2}$$

$$D^k_{rst\alpha\beta\gamma}(u) = \int_{\aleph^3} \bar{\phi}^k_{rst}(\xi, \zeta, \chi)\frac{\partial\phi^k_{\alpha\beta\gamma}(\xi, \zeta, \chi)}{\partial x}\left|J^k(\xi, \zeta, \chi)\right| \, \mathrm{d}\xi \, \mathrm{d}\zeta \, \mathrm{d}\chi, \tag{A3}$$

$$D^k_{rst\alpha\beta\gamma}(v) = \int_{\aleph^3} \bar{\phi}^k_{rst}(\xi, \zeta, \chi)\frac{\partial\phi^k_{\alpha\beta\gamma}(\xi, \zeta, \chi)}{\partial y}\left|J^k(\xi, \zeta, \chi)\right| \, \mathrm{d}\xi \, \mathrm{d}\zeta \, \mathrm{d}\chi, \tag{A4}$$

$$D^k_{rst\alpha\beta\gamma}(w) = \int_{\aleph^3} \bar{\phi}^k_{rst}(\xi, \zeta, \chi)\frac{\partial\phi^k_{\alpha\beta\gamma}(\xi, \zeta, \chi)}{\partial z}\left|J^k(\xi, \zeta, \chi)\right| \, \mathrm{d}\xi \, \mathrm{d}\zeta \, \mathrm{d}\chi, \tag{A5}$$

$$\begin{aligned} G^k_{ijl}(u) = {} & \frac{1}{2}(u^k_{mnp})^2\frac{\partial\phi^k_{mnp}(\xi_m, \zeta_n, \chi_p)}{\partial x} + v^k_{ijl}u^k_{mnp}\frac{\partial\phi^k_{mnp}(\xi_m, \zeta_n, \chi_p)}{\partial y} \\ & + w^k_{ijl}u^k_{mnp}\frac{\partial\phi^k_{mnp}(\xi_m, \zeta_n, \chi_p)}{\partial z}, \end{aligned} \tag{A6}$$

$$\begin{aligned} G^k_{ijl}(v) = {} & \frac{1}{2}(v^k_{mnp})^2\frac{\partial\phi^k_{mnp}(\xi_m, \zeta_n, \chi_p)}{\partial y} + u^k_{ijl}v^k_{mnp}\frac{\partial\phi^k_{mnp}(\xi_m, \zeta_n, \chi_p)}{\partial x} \\ & + w^k_{ijl}v^k_{mnp}\frac{\partial\phi^k_{mnp}(\xi_m, \zeta_n, \chi_p)}{\partial z}, \end{aligned} \tag{A7}$$

$$G^k_{ijl}(w) = \frac{1}{2}(w^k_{mnp})^2\frac{\partial\phi^k_{mnp}(\xi_m, \zeta_n, \chi_p)}{\partial z} + u^k_{ijl}w^k_{mnp}\frac{\partial\phi^k_{mnp}(\xi_m, \zeta_n, \chi_p)}{\partial x}$$

$$+ v^k_{ijl} w^k_{mnp} \frac{\partial \phi^k_{mnp}(\xi_m, \zeta_n, \chi_p)}{\partial y}, \tag{A8}$$

$$i, \alpha, m \in (0, \ldots, N_\xi), \quad j, \beta, n \in (0, \ldots, N_\zeta), \quad l, \gamma, p \in (0, \ldots, N_\chi)$$
$$r \in (1, \ldots, N_\xi - 1), \quad s \in (1, \ldots, N_\zeta - 1), \quad t \in (1, \ldots, N_\chi - 1)$$

and J is the transformation Jacobian,

$$J^k(\xi, \zeta, \chi) = \frac{\partial(\xi, \zeta, \chi)}{\partial(x, y, z)} = \begin{vmatrix} \dfrac{\partial x}{\partial \xi} & \dfrac{\partial x}{\partial \zeta} & \dfrac{\partial x}{\partial \chi} \\ \dfrac{\partial y}{\partial \xi} & \dfrac{\partial y}{\partial \zeta} & \dfrac{\partial y}{\partial \chi} \\ \dfrac{\partial z}{\partial \xi} & \dfrac{\partial z}{\partial \zeta} & \dfrac{\partial z}{\partial \chi} \end{vmatrix}, \quad (x, y, z) \in \Omega_k. \tag{A9}$$

All the integrations in the above equations are calculated by the Gauss–Lobatto quadrature rule (3.12) in the (ξ, ζ, χ) directions. The x, y and z derivatives in (A1)–(A8) can be expressed in terms of derivatives with local co-ordinates ξ, ζ and χ, according to the formula

$$\begin{pmatrix} \dfrac{\partial}{\partial x} \\ \dfrac{\partial}{\partial y} \\ \dfrac{\partial}{\partial z} \end{pmatrix} = \frac{1}{J} \begin{pmatrix} y_\zeta z_\chi - y_\chi z_\zeta & x_\chi z_\zeta - x_\zeta z_\chi & x_\zeta y_\chi - x_\chi y_\zeta \\ y_\chi z_\xi - y_\xi z_\chi & x_\xi z_\chi - x_\chi z_\xi & x_\chi y_\xi - x_\xi y_\chi \\ y_\xi z_\zeta - y_\zeta z_\xi & x_\zeta z_\xi - x_\xi z_\zeta & x_\xi y_\zeta - x_\zeta y_\xi \end{pmatrix} \begin{pmatrix} \dfrac{\partial}{\partial \xi} \\ \dfrac{\partial}{\partial \zeta} \\ \dfrac{\partial}{\partial \chi} \end{pmatrix}, \tag{A10}$$

where $x_\xi = \partial x / \partial \xi$, etc.

REFERENCES

1. O. Reynolds, ‘On the theory of lubrication and its application to Mr. Beauchamp Tower's experiments’, *Phil. Trans. R. Soc.*, **177**, 157–234 (1886).
2. D.Rh. Gwynllyw, A.R. Davies and T.N. Phillips, ‘On the effects of a variable viscosity lubricant on the dynamics of a journal bearing’, *J. Rheol.*, **40**, 1239–1266 (1996).
3. J.F. Barnes, J.F. Hutton and K. Walters, *An Introduction to Rheology*, Elsevier, Amsterdam, 1989.
4. A.R. Davies and X.K. Li, ‘Numerical modelling of pressure and temperature effects in viscoelastic flow between eccentrically rotating cylinders’. *J. Non-Newtonian Fluid Mech.*, **54**, 331–350 (1994).
5. J.F. Hutton, B. Jones and T.W. Bates, ‘Effects of isotropic pressure on the high temperature high shear viscosity of motor oils’, *Soc. Automot. Eng.* Paper No. 830030 (1983).
6. A.T. Patera, ‘A spectral element method for fluid dynamics: laminar flow in a channel expansion’, *J. Comput. Phys.*, **54**, 468–488 (1984).
7. Y. Maday and A.T. Patera, ‘Spectral element methods for the incompressible Navier–Stokes equations’, in A.K. Noor and J.T. Oden (eds.), *State of the Art Surveys in Computational Mechanics*, The American Society of Mechanical Engineers, New York, 1989, pp. 71–143.
8. R. Temam, *Navier–Stokes Equations and Nonlinear Functional Analysis*, SIAM, 1983.
9. W.J. Gordon and C.A. Hall, ‘Construction of curvilinear coordinate systems and application to mesh generation’, *Int. J. Numer. Meth. Eng.*, **7**, 461–477 (1973).
10. D.Rh. Gwynllyw and T.N. Phillips, ‘Preconditioned iterative methods for unsteady non-Newtonian flow between eccentrically rotating cylinders’, *SIAM J. Sci. Comput.*, **17**, 1369–1394 (1996).
11. G.W. Roberts, A.R. Davies and T.N. Phillips, ‘Three-dimensional spectral approximation to Stokes flow between eccentrically rotating cylinders’, *Int. J. Num. Methods in Fluids*, **13**, 217–223 (1991).

12. A. Cameron, *Basic Lubrication Theory*, Ellis Horwood, Chichester, 1981.
13. D. Dowson and C.M. Taylor, ‘Cavitation in bearings’, *Ann. Rev. Fluid Mech.*, **11**, 35–66 (1979).
14. D.Rh. Gwynllyw, A.R. Davies and T.N. Phillips, ‘A moving spectral element approach to the dynamically loaded journal bearing problem’, *J. Comput. Phys.*, **123**, 478–494 (1996).
15. J. Brindley, L. Elliott and J.T. McKay, ‘The role of cavitation in whirl instability in a rotor bearing’, *ASME J. Appl. Mech.*, **50**, 877–890 (1983).
16. A. Rastogi and R.K. Gupta, ‘Lubricant elasticity and the performance of dynamically loaded short journal bearings’, *J. Rheol.*, **34**, 1337–1356 (1990).